Fabrication of $CaAl_{12}O_{19}$-$CaTiO_3$ composites and their potential usage for TiAl alloy smelting

Abstract

$CaAl_{12}O_{19}$-$CaTiO_3$ (CA_6-CT) materials are fabricated using a solid sintering method to investigate the effects of the calcium source and TiO_2 content on the phase composition, properties, and microstructure of the materials. The type of calcium source plays a crucial role in determining the reactivity and sintering behavior of the composite materials. Compared to $CaCO_3$ micropowder and $Ca(OH)_2$ micropowder, nano $CaCO_3$ is the preferred calcium source for fabricating composite materials with a better degree of sintering and well-grown CA_6 grains. The sintering activity of the material is significantly improved by increasing the TiO_2 content. The preferential replacement of Al^{3+} by Ti^{4+} in the mirror layer of the CA_6 crystal increases the concentration of vacancy defects in the layer, thereby promoting ion diffusion and mass transfer, which improves the sintering reaction activity. However, as more TiO_2 is added, the $CaTiO_3$ phase formed increases the thermal conductivity and mean expansion coefficient of the material at high temperatures, which degrades its thermal shock stability. The CA_6-CT refractory showed good corrosion resistance to the Ti6Al4V melt. Except for a slight penetration of iron element, no obvious corrosion occurred at the reaction interface.

Keywords: Calcium hexaluminate, Calcium titanate, TiAl alloy, Sintering behaviour, Reaction interface

1 Introduction

The alloys have an extremely broad range of applications. They could be used as the basic structural materials (medical devices, transport equipment, building materials, etc.) or advanced functional materials (phase change heat storage material, catalysts, energy storages materials, sensors, absorbing materials, etc.). Owing to their low specific gravity, high specific strength, large hydrogen storage capacity, low damping, good biocompatibility, and shape memory, titanium alloys have been widely employed in energy storage, sensing, aerospace and healthcare industries [1–5]. Among the various titanium alloys, TiAl alloys possess low density and high specific strength, specific stiffness, and resistance to high-temperature creep and oxidation. They are the preferred materials for ultra-high-speed aircraft and the next generation of advanced aircraft engines.

Currently, the vacuum induction furnace is an important smelting equipment for producing titanium alloys, nickel-based superalloys, stainless steel, and ultra-high-strength steel [6]. Compared to other common electric furnaces, it has the advantages of a fast heating rate, high production efficiency, and reduced oxidation loss. Electromagnetic stirring can provide good degassing and alloy homogenization, which improves mechanization and automation [7]. However, compared with other commonly used alloys, the fabrication of TiAl alloys requires higher processing temperatures (above 1600 °C), indicating a higher chemical activity of the molten alloy [8,9]. In this case, the

alloy melt reacts heavily with the refractory crucible, resulting in impurities, inclusions, and casting defects in the produced alloy.

Kostov et al. [10] calculated the dissolution Gibbs free energies of various oxides (Y_2O_3, ZrO_2, CaO, Al_2O_3, MgO, and SiO_2) in TiAl alloys with different titanium contents and found that only Y_2O_3, CaO, ZrO_2, and Al_2O_3 are suitable crucible materials for melting titanium and its alloys. However, Y_2O_3 crucibles have poor thermal shock resistance, whereas the application of CaO crucibles is greatly limited by the hydration of CaO in practical applications [11–14]. The solid solution of ZrO_2 in titanium usually leads to a high oxygen content in the alloy [15]. Although Al_2O_3 crucibles have good corrosion resistance to TiAl alloys with high aluminum content, their resistance to alloys with low aluminum content is still unsatisfactory [16]. In recent years, zirconate refractories ($CaZrO_3$ and $BaZrO_3$) have been produced by Chen et al.[17] and Schafföner et al.[18] for vacuum induction melting of titanium alloys. Although zirconate refractories possess high melting points and good high-temperature stability, they are brittle and exhibit poor thermal shock resistance during service [19,20]. Therefore, the key challenge in the smelting of pure TiAl alloys is in the development of reliable refractory crucibles.

In the CaO-Al_2O_3-TiO_2 (CA_6-CT) system, $CaAl_{12}O_{19}$ and $CaTiO_3$ have the highest stability. Moreover, they have high refractoriness and corrosion resistance and thermal shock stability [21–24]. Therefore, in this study, $CaAl_{12}O_{19}$-$CaTiO_3$ composite materials were fabricated using a solid sintering method. The effects of the calcium source and TiO_2 content on the phase composition, properties, and microstructure of the CA_6-CT

materials were investigated in detail. Finally, the potential application of CA_6-CT materials for the smelting of titanium aluminum alloys was assessed.

2 Experimental

2.1 Starting materials

Three different calcium sources, α-Al_2O_3 micropowder, and TiO_2 were used as the raw materials. α-Al_2O_3 with an alumina content ≥ 99 wt% and median particle size < 3 μm was provided by Jiangsu Jingxin New Materials Co., Ltd.. The three calcium sources were $Ca(OH)_2$ micropowder, $CaCO_3$ micropowder, and nano $CaCO_3$. Nano $CaCO_3$ with a $CaCO_3$ content ≥ 96% and median particle size < 80 nm was obtained from Zhejiang Changshan Jinxiong Co., Ltd.. The $Ca(OH)_2$ and $CaCO_3$ micropowder were produced by Shanghai McLin Biochemical Technology Co., Ltd and had a $Ca(OH)_2$ content ≥ 95 % and $CaCO_3$ content ≥ 99 %, respectively.

2.2 Sample preparation

The raw materials were weighed according to the experimental formula. 60 wt% water was added to each raw material, which was wet-mixed using a planetary ball mill at a ball-to-material mass ratio of 6:1 and speed of 258 r/min. The uniformly mixed slurry was dried at 110 °C in a blast-drying oven and then crushed into a fine powder. 1 wt.% polyvinyl alcohol (PVA solution, 10 wt. % concentration) was added as a binder. After the powder and binder were mixed evenly, a Φ 20 mm cylindrical sample was prepared under 150 MPa uniaxial pressure and dried at 80 °C and 110 °C for 24 h. Finally, the

dried green body was heat-treated at 1650 °C for 3 h.

After determining the optimal calcium source, the proportion of TiO_2 in the ternary system was adjusted. The samples were dried by molding and sintered at 1300, 1400, 1500, 1600, 1650, or 1700 °C for 3 h in a silicon–molybdenum rod furnace.

2.3 Characterization

The dimensions of the samples before and after sintering were measured to calculate the linear shrinkage. The volume densities and apparent porosities of the samples were measured using the Archimedes method. The phase compositions of the samples were analyzed using X-ray diffraction (X'pert Pro (Cu Kα), Philips, Netherlands). The surface morphology and microstructure of the samples were observed using field-emission scanning electron microscopy (FEI Nova 400 Nano-SEM, FEI, USA) and the elemental analysis of the micro-area composition performed using an X-ray energy spectrometer (INCA Penta FET-X3, Oxford Instruments, UK). The linear thermal expansion coefficient of the sample was measured using a high-temperature thermal dilatometer (Unitherm^{TM} model 1161, Ant, USA) at temperatures ranging from room temperature to 1400 °C at a heating rate of 5 °C/min. The thermal conductivities of the samples at various temperatures were measured using a laser thermal conductivity meter (LFA 457 MicroFlash, Niche Instruments, Germany).

3 Results and discussion

3.1 Effect of Ca source on synthesis and properties of CA_6-CT materials

The molar ratio of $CaO:Al_2O_3:TiO_2$ of 1.70:5.04:0.48 used in the experimental samples is located within the $CaTiO_3$-$CaAl_4O_7$-$CaAl_{12}O_{19}$ triangle region (Fig. 1). The $CaCO_3$ micropowder, nano $CaCO_3$, and $Ca(OH)_2$ micropowder were used as calcium sources. The samples produced using the three calcium sources are denoted as C1, C2, and C3, respectively. The prepared samples were heat-treated at 1650 °C for 3 h. Table 1 shows the compositions of the three groups of samples.

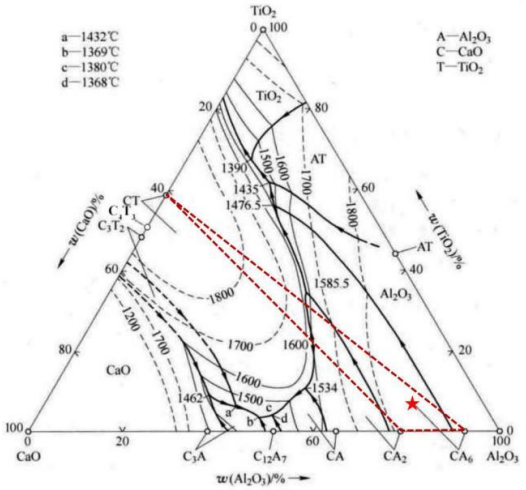

Fig. 1 CaO-Al_2O_3-TiO_2 ternary diagram.

Table 1 Composition of samples (wt%).

Sample	C1	C2	C3
α-Al_2O_3 micropowder	71.17	71.17	76.07
$CaCO_3$ micropowder	24.23	—	—
Nano $CaCO_3$	—	24.23	—
$Ca(OH)_2$ micropowder	—	—	19.16
TiO_2	4.60	4.60	4.77

Fig. 2 shows the XRD patterns of the three sample groups. The phases of the samples prepared using the three calcium sources were $CaAl_{12}O_{19}$, $CaAl_4O_7$, and $CaTiO_3$, respectively. Based on the diffraction peak strength of the phase, the relative content of

each phase was calculated using the reference strength method (RIR) and shown in Table 2. The three groups had similar $CaTiO_3$ phase contents. The ratio of the CA_6 to CA_2 phases was the largest in the C2 samples, followed by the C3 and C1 samples in turn. For a given composition ratio, a larger CA_6 to CA_2 phase ratio indicates a greater degree of transformation from CA_2 to CA_6. Therefore, the reactant activity in C2 was greater than those in C3 and C1 under 1650 °C heat treatment.

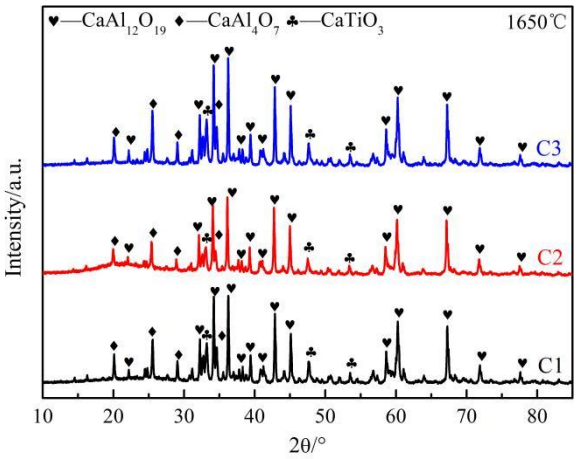

Fig. 2 XRD patterns of samples.

Table 2 Phase composition of samples with different calcium sources (wt%).

Sample	$CaAl_{12}O_{19}$	$CaAl_4O_7$	$CaTiO_3$
C1	59	32	9
C2	72	21	7
C3	66	27	7

Fig. 3 shows the microstructures of the samples sintered at 1650 °C. The pores were uniformly distributed in the three groups of samples, and no obvious large pores were observed. The pores in C2 and C3 were small, and the number of pores in C3 was relatively small. The statistics of the measured pore diameters indicate that the average pore diameter (D_a) and median pore diameter (D_{50}) in C2 were smaller than those in the

other two groups. Equations (1) and (2) show that $Ca(OH)_2$ begins to decompose at approximately 400 °C, and $CaCO_3$ decomposes completely at approximately 900 °C. Therefore, the gas in C3 had a longer time to discharge, resulting in fewer pores after sintering. Meanwhile, the relatively small pores remaining after the decomposition of nano-$CaCO_3$ provided sufficient space for the growth of CA_6 grains in the C2 samples. However, the excessive pores in C1 may have hindered material transfer between the oxides and were not conducive to the solid-state reactions.

$$CaCO_3(s) \xrightarrow{590\sim753°C} CaO(s) + CO_2(g) \quad (1)$$

$$Ca(OH)_2(s) \xrightarrow{400\sim600°C} CaO(s) + H_2O(g) \quad (2)$$

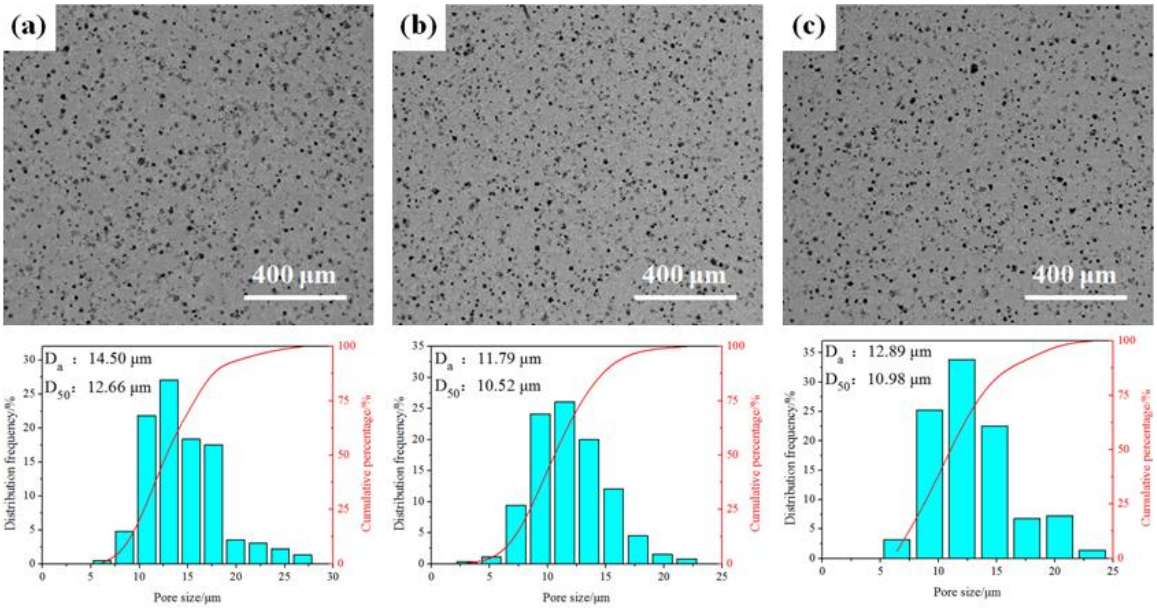

Fig. 3 SEM images of samples: (a) C1; (b) C2; (c) C3.

Fig. 4 shows the microstructures of the samples fired with different calcium sources. Grains with a hexagonal flake morphology were observed in the three groups of samples. The energy spectrum results listed in Table 3 indicate that the plate-like grains in the

samples were CA_6 (points 1 and 4) and a small amount of titanium was dissolved in the CA_6 grains. Most of the TiO_2 reacted with CaO to form $CaTiO_3$, which filled the spaces between the CA_6 grains. In addition, the CA_6 was intercalated by rod-like CA and CA_2 grains. By comparing Fig. 4 (b), (d), and (f), it can be seen that in the samples in which micro-$CaCO_3$ and $Ca(OH)_2$ were used as calcium sources (C1 and C3), the CA_6 and CA_2 grains had rough surfaces and were covered by a scale-like substance. In the sample in which nano-$CaCO_3$ was used as the calcium source (C2), the surfaces of the particles were relatively flat and had no similar microscopic morphology to those of the C1 and C3 samples. Combined with the XRD results, it can be concluded that there were no significant differences in the reaction products between the three groups. It is speculated that the activity of CaO produced by decomposition was slightly lower when micro $CaCO_3$ and $Ca(OH)_2$ were used as the calcium sources. After heat treatment at 1650 °C for 3 h, a small amount of unreacted intermediate products such as CA remained in the sample and were hydrated during the sample preparation process. These results also show that the CaO obtained after the decomposition of nano $CaCO_3$ had higher reactivity and could react more easily to form a larger amount of CA_6 and $CaTiO_3$ phases compared to the other two calcium sources.

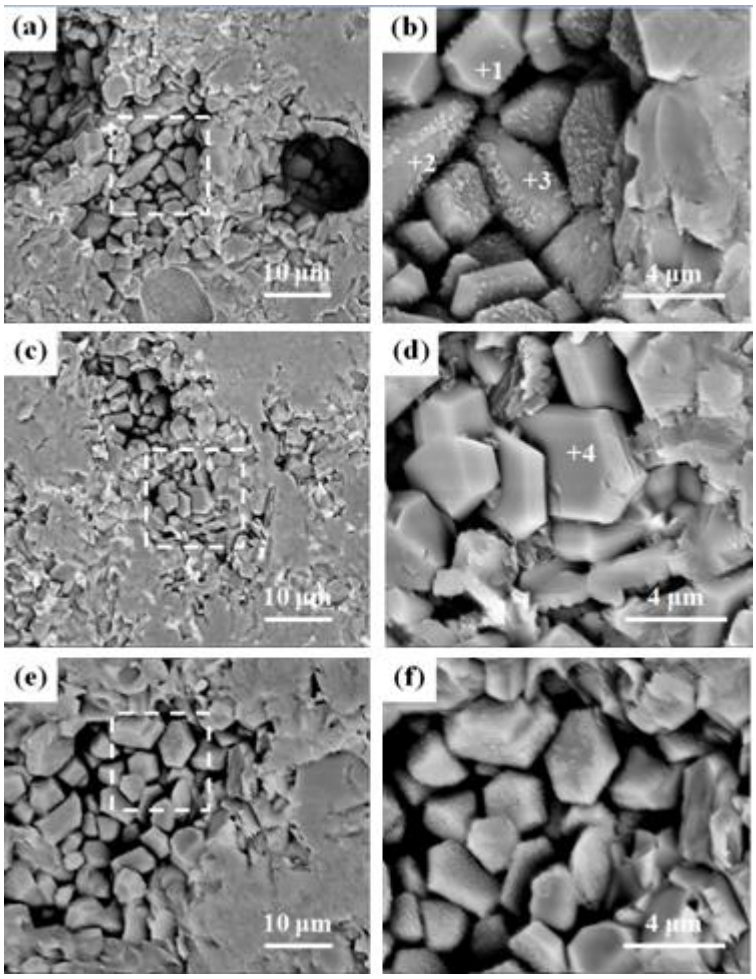

Fig. 4 SEM images of samples: (a) and (b), C1; (c) and (d), C2; (e) and (f), C3.

Table 3 EDS analysis of points in Fig. 4 (at%).

Point	Ca	Al	Ti	O	Possible phase
1	4.1	39.2	0.8	56.0	CA_6
2	6.9	30.5	0.1	62.5	CA_2
3	19	34.1	0.3	46.6	CA
4	6.9	54.8	1.5	36.7	CA_6

The sintering properties of the three groups of samples are shown in Fig. 5. The linear shrinkage rate of the C2 samples was higher than those of the other two groups, whereas only small differences existed between the bulk densities and apparent porosities

of the three sample groups. The bulk density and apparent porosity of C2 were 3.19 g/cm^3 and 8.8 %, respectively. When nano $CaCO_3$ was used as the calcium source (C2), the CaO particles produced by decomposition had smaller sizes, larger specific surface areas, and higher activity compared to those produced from the other calcium sources. These factors promoted the sintering reaction of the sample at high temperatures and increased its radial shrinkage.

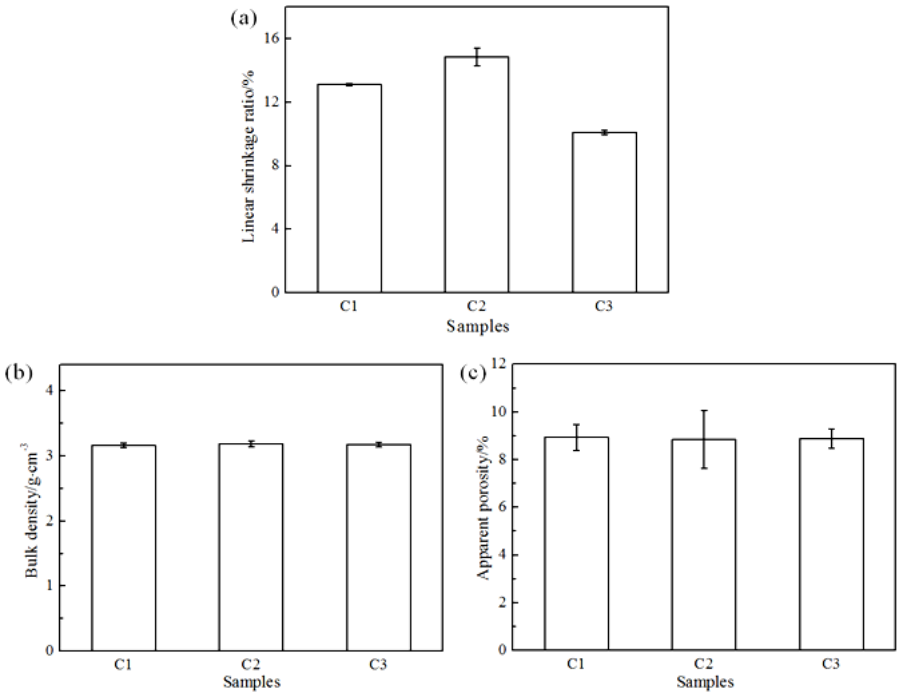

Fig. 5 Sinter properties of samples: (a) linear shrinkage; (b) bulk densities; (c) apparent porosity.

The aforementioned results show that the sample in which nano $CaCO_3$ was used as the calcium source underwent a better degree of sintering. The higher reaction activity of the raw material facilitated grain growth in the CA_6-CT material. Therefore, nano $CaCO_3$ was used as the calcium source in the subsequent experiments.

3.2 Effect of TiO_2 content on phase and structure of CA_6-CT materials

The molar ratios of $CaO:Al_2O_3:TiO_2$ in the samples were set to 1.7:5.04:0, 1.7:5.04:0.48, 1.7:5.04:0.96, and 1.7:5.04:1.44 by adjusting the proportion of TiO_2 in the ternary system based on nano $CaCO_3$, which was used as the calcium source. The composition points are denoted as T0, T1, T2, and T3, respectively. The positions of the composition points in the phase diagram are shown in Fig. 6, and the compositions of the raw materials in Table 4. After molding and drying, the samples were placed in a silicon–molybdenum rod furnace and sintered at 1300, 1400, 1500, 1600, 1650, or 1700 °C for 3 h.

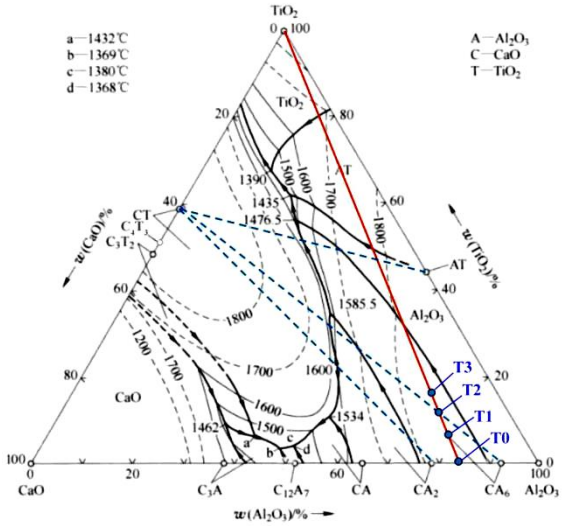

Fig. 6. CaO-Al_2O_3-TiO_2 ternary diagram.

Table 4 Initial composition of samples (wt%).

Sample	T0	T1	T2	T3
α-Al_2O_3	75.2	71.2	67.5	64.3
Nano $CaCO_3$	24.8	23.5	22.4	21.3
TiO_2	0	5.3	10.1	14.4

The XRD results for the four groups of samples after heat treatment at 1700 °C are

shown in Fig. 7. In the T0 sample without TiO_2, the CaO content was relatively surplus, and the phases were CA_2 and CA_6. The diffraction peak of the $CaTiO_3$ phase was observed in the T1 sample after adding 5.3 wt. % TiO_2. As more TiO_2 was added, the CA_2 phase disappeared, and the relative strength of the $CaTiO_3$ diffraction peak increased initially and then decreased. The diffraction peak of $Ca_3Ti_8Al_{12}O_{37}$ was observed in the T3 sample.

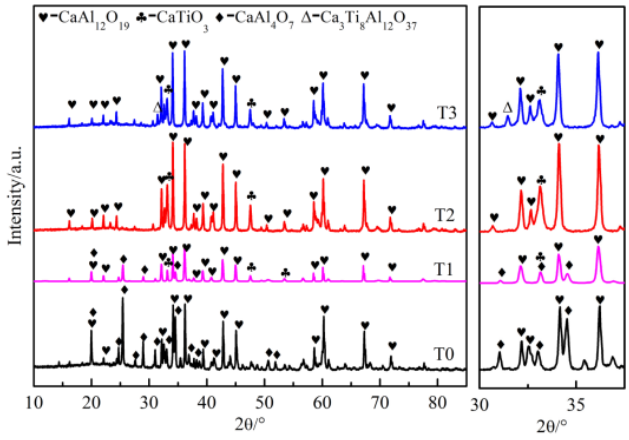

Fig. 7 XRD patterns of samples after heat treatment at 1700 °C.

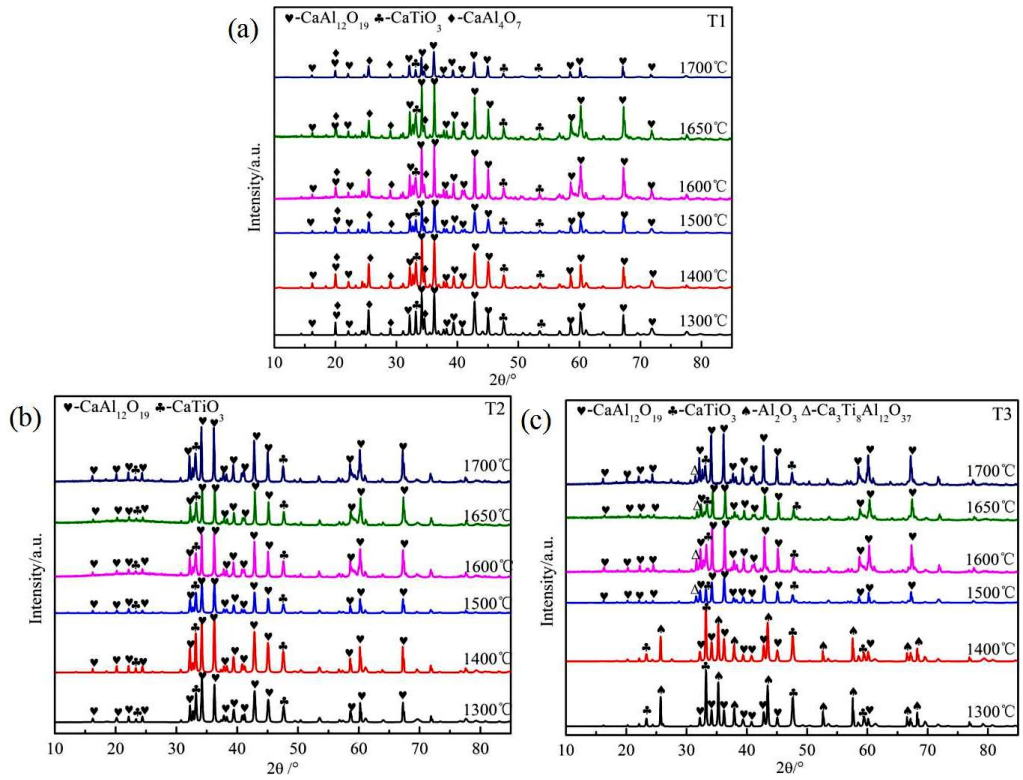

Fig. 8. XRD patterns of samples after heat treatment at different temperatures: (a) T1; (b) T2; (c) T3.

Fig. 8 shows the XRD patterns of the T1, T2, and T3 samples after heat treatment at different temperatures. The main phases in the T1 sample were CA_6, CA_2, and $CaTiO_3$. As the temperature increased, the gradual decrease in the intensities of the CA_2 and $CaTiO_3$ diffraction peaks indicates an ongoing conversion of CA_2 to CA_6. The phases of the T2 sample after sintering at 1300 °C were CA_6 and $CaTiO_3$. The small changes in the phase composition and relative intensities of the diffraction peaks with temperature indicate that the synthesis reaction of CA_6 and $CaTiO_3$ tended to be completed at low temperatures when the T2 sample formula was used. The main processes that occurred above 1300 °C were crystal growth and sintering. In the T3 sample, the α-Al_2O_3 phase

was enriched because of the excess TiO_2 added at the beginning of the reaction. Below 1400 °C, α-Al_2O_3 and $CaTiO_3$ were the main phases. As the temperature increased, the relative intensity of the CA_6 diffraction peak increased gradually and the decomposition of $CaTiO_3$ produced free TiO_2, which underwent the reaction in Equation (3) and resulted in the $Ca_3Ti_8Al_{12}O_{37}$ phase diffraction peak.

$$3CaO + 6Al_2O_3 + 8TiO_2 \longrightarrow Ca_3Ti_8Al_{12}O_{37} \quad (3)$$

It can be seen from the XRD patterns that CA_6 and $CaTiO_3$ phases were formed in the three groups of samples at 1700 °C. At low temperatures, the T1 and T3 samples contained obvious CA_2 and α-Al_2O_3 phases, which decreased with increasing temperature. $CaCO_3$ usually decomposes to CaO at 590–753 °C [25], which then reacts with α-Al_2O_3 to form calcium aluminate phases (C_3A, $C_{12}A_7$, CA) with low melting points. Despite the low formation temperature of CA, $CaTiO_3$ is formed preferentially above 1300 °C, and the remaining CaO continues to react with Al_2O_3 to form CA_6. It should be noted that $CaTiO_3$ is less stable than CA_6 at high temperatures (> 1500 °C); therefore, $CaTiO_3$ may decompose into the CA_6 phase when Al_2O_3 is enriched.

Fig. 9 shows the SEM images of the T1 samples after heat treatment at 1300–1700 °C for 3 h. After heat treatment at 1300 °C for 3 h, $CaCO_3$ decomposed leaving many connected pores in the sample. Combining these observations with the energy spectrum analysis and XRD results in Table 5, the atomic ratio of the lamellar grains was

observed to be between those of CA_2 and CA_6, indicating that CA_6 has begun to form at this temperature. $CaTiO_3$ was distributed between the CA_6 aggregates in the form of particles. After heat treatment at 1400 °C, the CA_2 and CA_6 grains grew obviously, the formed CA_6 grains began to overlap, and the sample changed from expansion to contraction. In the 1500 °C T1 sample, the porosity was significantly reduced, the CA_6 developed a plate-like morphology, and a small amount of $CaTiO_3$ formed in the grain gaps. As the heat treatment temperature increased further, the CA_2 and CA_6 grains continued to grow, and the CA_6 grains tended toward an equiaxed morphology. After heat treatment at 1700 °C, the gaps between the CA_6 grains increased. It is speculated that at this temperature, CA_2 underwent inconsistent melting. This caused the gaps to increase because the decomposed liquid phase that filled the inter-grain gaps shrunk and left gaps as it cooled and crystallized.

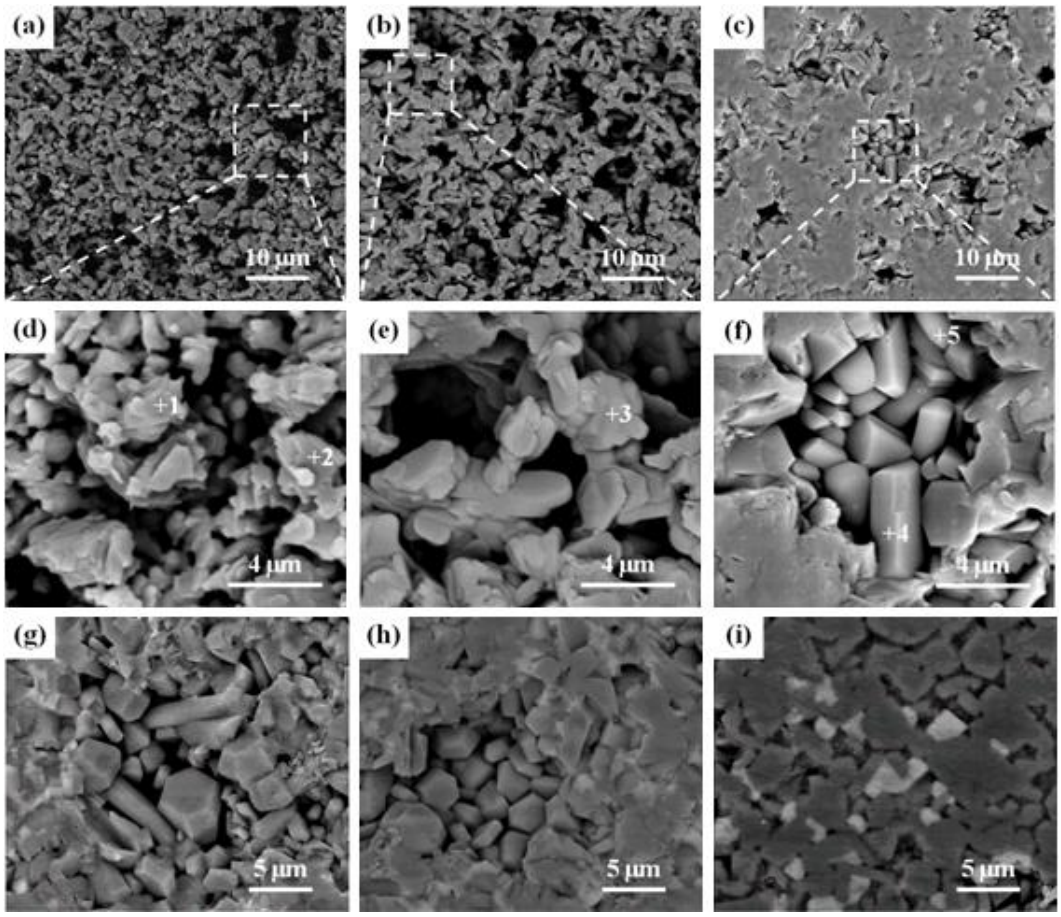

Fig. 9 SEM images of T1 sample: (a) and (d) 1300 °C; (b) and (e) 1400 °C; (c) and (f) 1500 °C; (g) 1600 °C; (h) 1650 °C; (i) 1700 °C.

Table 5 EDS analysis of points in Fig. 3.8 (at%).

Point	Ca	Al	Ti	O	Possible phases
1	4.0	35.1	0.7	60.2	CA_6
2	7.7	19.1	5.9	67.3	CA_2
3	4.6	44.0	2.2	49.2	CA_6
4	3.0	35.9	0.7	60.4	CA_6
5	23.8	12.5	23.8	39.9	$CaTiO_3$

Fig. 10 shows the SEM images of the T2 samples after heat treatment at different temperatures for 3 h. Unlike the T1 sample, no CA_2 grains were observed in the T2 sample. After heat treatment at 1400 °C, the $CaTiO_3$ particles adhered to the CA_6 flakes,

the CA_6 was in the initial stage of growth. The grains were thin with hexagonal growth base surfaces, and they overlapped with one another to form a network structure. $CaTiO_3$, which has a shallower contrast in the images, had an irregular shape and was dispersed in the matrix. No agglomeration was observed. The grains grew as the temperature increased. Above 1500 °C, the density of the sample increased significantly, and some CA_6 grains continued to grow along the thickness direction. As shown in Fig. 3.9 (i), $CaTiO_3$ filled the spaces between the CA_6 grains and exhibited good bonding with the surrounding grains.

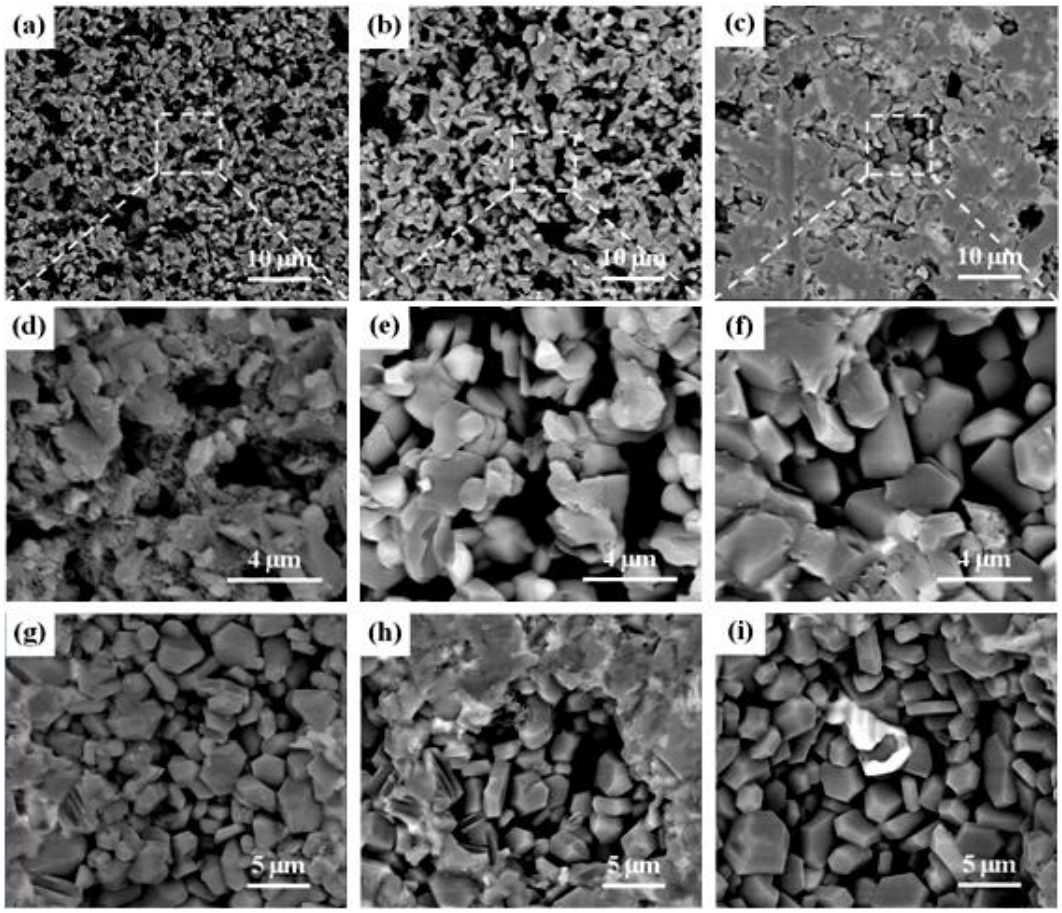

Fig. 10 SEM images of T2 sample: (a) and (d) 1300 °C; (b) and (e) 1400 °C; (c) and (f) 1500 °C; (g) 1600 °C; (h) 1650 °C; (i) 1700 °C.

Fig. 11 shows the SEM images of the T3 sample after heat treatment at different temperatures for 3 h. At the beginning of the sintering process, a large amount of TiO_2 reacted with CaO, resulting in the enrichment of Al_2O_3. $CaTiO_3$ was located between lamellar α-Al_2O_3 after sintering at 1300 °C (Fig. 11 (d)). Because $CaTiO_3$, which has a high density, was almost formed in the sample and filled some pores left by $CaCO_3$ decomposition, the bulk density of the sample was larger than those of the other groups, and a certain shrinkage was produced. Between 1300 and 1400 °C, $CaTiO_3$ began to react with α-Al_2O_3 to form CA_6. Together with the energy spectrum analysis results in Table 6, it can be concluded that some CA_6 grains in the T3 sample exhibited an equiaxed morphology (Fig. 11 (f)) and a certain amount of Ti^{4+} formed a solid solution. The presence of $Ca_3Ti_8Al_{12}O_{37}$ was clearly observed in the sample after heat treatment at 1600 °C (point 3). Although Ti^{4+} did not completely participate in the solid solution during the formation of CA_6, the rich TiO_2 that resulted in $CaTiO_3$ decomposition participated in the reaction in Equation (3) and generated $Ca_3Ti_8Al_{12}O_{37}$, which filled the gaps and the resultant pores in the CA_6 grains.

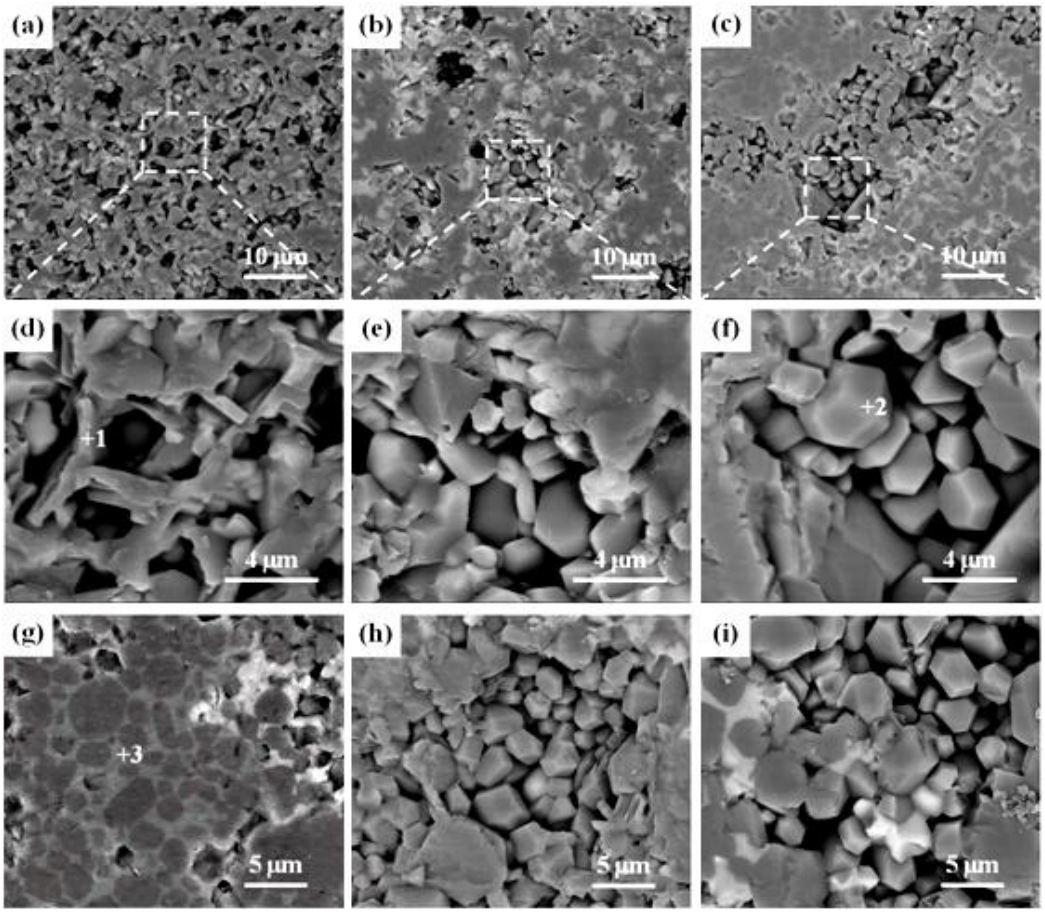

Fig. 11 SEM images of T3 sample: (a) and (d) 1300 °C; (b) and (e) 1400 °C; (c) and (f) 1500 °C; (g) 1600 °C; (h) 1650 °C; (i) 1700 °C.

Table 6 EDS analysis of points in Fig. 11 (at%).

Point	Ca	Al	Ti	O	Possible phase
1	0.9	33.7	0.9	64.4	Al_2O_3
2	3.7	38.3	1.0	57.0	CA_6
3	3.9	32.1	9.3	54.7	$Ca_3Ti_8Al_{12}O_{37}$

By comparing the grain morphologies of the T1, T2, and T3 samples, it can be seen that as the TiO_2 content increased, CA_6 gradually developed from a plate-like structure to an equiaxed morphology. Based on the earlier analysis, this change can be attributed to following: the $CaTiO_3$ and $Ca_3Ti_8Al_{12}O_{37}$ produced in the sample hindered the growth of

the CA_6 crystal along the basal plane while the pinning effect of the $CaTiO_3$ grain reduced the aspect ratio of CA_6.. Additionally, the $[CaAlO_3]^-$ mirror layer in the crystal structure of CA_6 is constituted by Ca^{2+}, which has a larger radius, and one Al^{3+}, and three O^{2-} ions. Because the mirror layer separates the $[Al_{11}O_{16}]^+$ spinel layers, it hinders the diffusion of O^{2-} along the parallel c-axis direction and results in anisotropic crystal development, which is reflected in the preferential growth of plate or flake grains. When TiO_2 was added to the material, the Ti^{4+} dissolved in CA_6 preferentially replaced Al^{3+} in the mirror layer of the CA_6 crystal and generated vacancies, which is equivalent to increasing the defect concentration in the mirror layer. As V_{Al} in the mirror layer increased, the increase in the vacancy concentration difference between the mirror and spinel layers promoted ion diffusion and mass transfer along the c-axis direction. This resulted in the tendency for the CA_6 grains to develop with an equiaxed morphology.

Fig. 12 shows the variation in the bulk densities and apparent porosities of the four groups of samples with temperature. Below 1650 °C, the T0 sample was in the grain growth and solid-state sintering stages, and its volume density increased from 1.6 g/cm^3 to 3.0 g/cm^3 as the temperature increased from 1300 to 1650 °C. When the temperature was extremely high (1700 °C), the sintering performance began to decline, indicating the occurrence of overburning. Below 1500 °C, the bulk densities of the T1 and T2 samples increased with the sintering temperature, and the porosity decreased accordingly. The bulk densities of the T1 and T2 samples after heat treatment at 1600 °C were 3.27 g/cm^3 and 3.35 g/cm^3, respectively, and their apparent porosities were 7.1 % and 11.8 %,

respectively. When the temperature increased to 1700 °C, the apparent porosities of the samples increased. At sintering temperatures below 1400 °C, the volume density of the T3 sample remained above 3.1 g/cm^3 and its apparent porosity below 20 % because of the large amount of α-Al_2O_3 phasesthat were not involved in the reaction. When the heat treatment temperature exceeded 1500 °C, α-Al_2O_3 reacted with $CaTiO_3$ to form CA_6, which developed into a hexagonal plate structure. The increased number of inter-grain pores resulted in the decrease of the bulk density from 3.7 g/cm^3 to 3.3 g/cm^3. Based on the aforementioned analysis, the appropriate heat treatment temperature is 1650 °C.

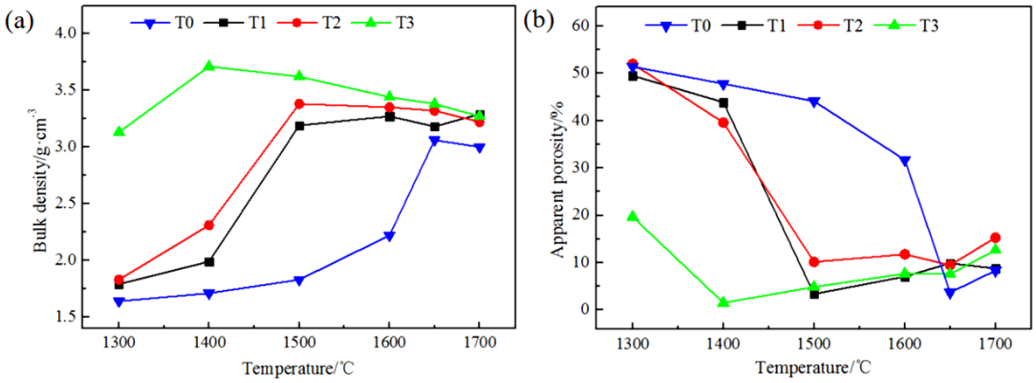

Fig. 12 Sinter properties of samples: (a) bulk density; (b) apparent porosity.

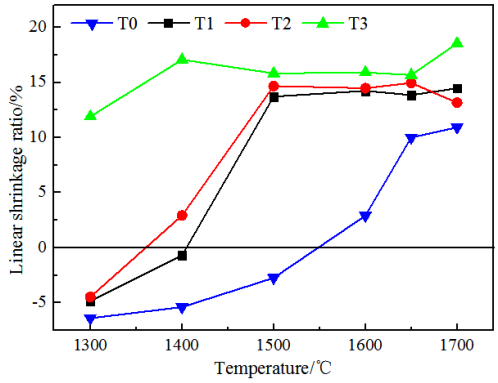

Fig. 13 Radial line shrinkage of samples.

Fig. 13 shows the influence of different heat treatment temperatures on the linear change rates of the four groups of samples. At a given temperature, the linear shrinkage rates of the samples increased after adding TiO_2. The T0 sample expanded below 1500 °C owing to the volume expansion caused by the formation of calcium aluminate (especially CA_2 and CA_6). In particular, the inhibition of intercrystalline ion diffusion by the network structure composed of CA_6 grains hindered pore discharging. However, the sample began to shrink after heat treatment at 1600 °C, indicating that it had reacted between 1500 and 1600 °C and completed the sintering reaction at approximately 1700 °C. The T1 and T2 samples shrunk at 1400 °C and remained stable above 1500 °C, indicating that the addition of TiO_2 significantly promoted the solid-state reaction and sintering process. After heat treatment at 1300 °C, the T3 sample shrunk. This is because the rich Al_2O_3 content connected to form a skeleton structure, which inhibited the anisotropic growth of CA_6. As the temperature increased further to 1500 °C and Al_2O_3 participated in the reaction, CA_6 began to grow, and the sample expanded slightly.

The heat capacity of a material reflects the change in the energy of the molecular thermal motion with temperature. A larger heat capacity results in a smaller increase in the temperature when the same amount of heat is absorbed by the material and is conducive to improving the thermal shock resistance of the material. Table 7 shows the specific heat capacities of the three groups of samples measured using the laser thermal conductivity instrument at different temperatures after heat treatment at 1650 °C. The

three groups of samples had similar specific heat capacities at 200 °C. The specific heat capacities increased with the temperature. When the temperature reached 1000 °C, the specific heat capacity of the T3 samples increased significantly. The specific heat capacities of the T2 and T3 samples were higher than those of the T1 samples.

Table 7 Specific heat capacities of samples.

Temperature/°C	T1	T2	T3
200	0.842	0.884	0.993
400	0.965	0.989	1.067
600	1.031	1.054	1.178
800	1.091	1.135	1.179
1000	1.07	1.837	4.438

Fig. 14 shows the thermal conductivities of the T1, T2, and T3 samples after heat treatment at 1700 °C. When the temperature was lower than 800 °C, the thermal conductivity of the three groups of samples decreased as the temperature increased. T3 exhibited the highest thermal conductivity, followed by T2 and T1 in turn. Above 800 °C, the thermal conductivities of the T2 and T3 samples began to increase, possibly because the thermal conductivity of air in the material pores and the radiation effect between the pore walls increased with the temperature. The thermal conductivities of the T1, T2 and T3 samples at 1000 °C were 2.17, 3.81, and 9.15 W/(m· K), respectively.

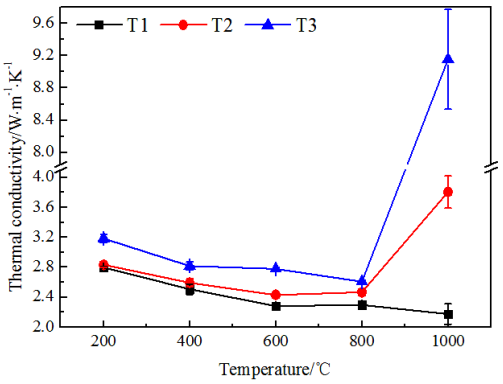

Fig. 14 Thermal conductivity of samples.

Table 8 Physical properties of typical refractories.

Material	Thermal conductivity /W·m^{-1}·K^{-1}	Average coefficient of linear expansion (20–1000 °C) /10^{-6}·°C^{-1}
Al_2O_3	28~35	8.0
CaO	30	15.2
ZrO_2	2.5	10.0
Y_2O_3	8~12	8.1
Graphite	140	0.6~5.2

Table 8 lists the physical properties of several common crucible refractories [26,27]. The thermal conductivity of the experimentally prepared CA_6-CT material was relatively low and between those of the ZrO_2 and Y_2O_3 refractories. A lower crucible thermal conductivity helps in reducing the cooling rate of the molten alloy and maintaining its superheating. The thermal conductivity of a material is affected by its chemical composition and microstructure. The relatively small atomic mass of $CaTiO_3$ and its cubic crystal structure, which is simpler than that of CA_6, contribute to a large thermal conductivity. However, a lower $CaTiO_3$ content in the CA_6-CT material corresponds to higher porosity between the CA_6 grains, which reduces the thermal conductivity of the material. Therefore, the T3 sample, which has the largest $CaTiO_3$ content, also has the

highest thermal conductivity.

It can be seen from Fig. 15 that in the temperature range 25–1200 °C, the linear expansion rate and average linear expansion coefficient of the three groups of samples increased with the temperature. The average linear expansion coefficients of the T2 and T3 samples were similar and larger than that of the T1 sample. The average linear expansion coefficient of the T1 sample was 7.9×10^{-6} / °C in the temperature range 25–1000 °C, which is similar to that of corundum (Table 8). Although the presence of $CaTiO_3$ in the sample increased its average linear expansion coefficient, the CA_2 phase in T1 belongs to the monoclinic system, which exhibited a relatively low average linear expansion coefficient ($\leq 5.6\times10^{-6}$/°C) in the temperature range 200–1200 °C. The average linear expansion coefficients of the three groups decreased above 1200 °C. The average linear expansion coefficient of a material is closely related to its heat capacity and has a similar variation; therefore, the average linear expansion coefficients of the T2 and T3 samples were not significantly different. In contrast, in the T1 sample, there were many pores between the hexagonal CA_6 grains. These pores were bridged first when the grains underwent thermal expansion. The resultant delay in the thermal expansion led to a small thermal expansion.

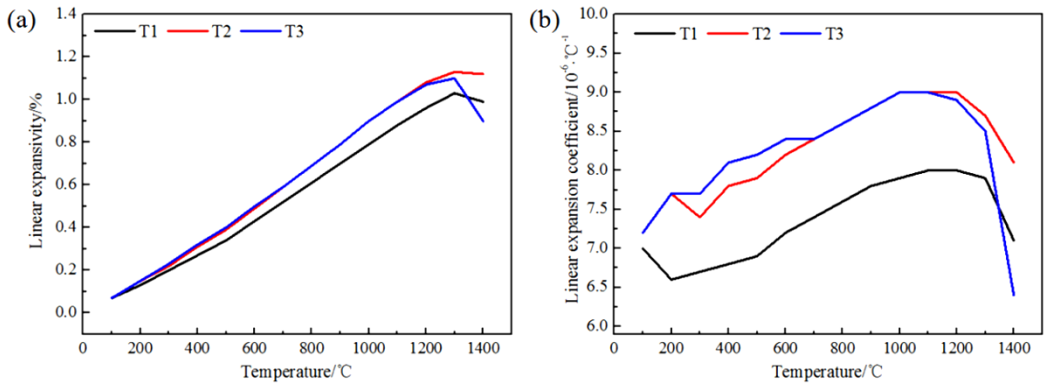

Fig. 15. (a) Linear expansion and (b) mean expansion coefficient versus temperature of samples.

3.3 Interfacial reaction between CA_6-CT refractories and TiAl melt

In order to assess the potential application of CA_6-CT materials for the smelting of titanium aluminum alloys, interfacial reaction between CA_6-CT refractories and TiAl melt were investigated. According to the initial compositions of sample T1 in Table 4, CA_6-CT refractory crucibles with a size of Φ50 mm × 50 mm (inner diameter Φ (12-15) mm × 15 mm) were fabricated after sintered at 1650 °C for 3 h. For the melting experiment, a commercial Ti6Al4V alloy (with a composition shown in Table 9) was selected. The Ti6Al4V alloy was put into the crucible and then placed in the VIM furnace. The furnace was evacuated and backfilled with high purity argon gas. Then the temperature in the furnace raised rapidly to above 1660 °C within 25 min. After the melt became visible, the alloy was further heated for 1 min. The furnace was then switched off and the samples were allowed to cool naturally to room temperature in the furnace.

Table 9 Chemical composition of Ti6Al4V alloy (wt.%).

Element	Ti	Al	V	Fe
Content	87.17	7.66	4.75	0.18

The reaction interface between CA_6-CT refractories and Ti6Al4V melt is shown in Fig. 16. No obvious corrosion occurred at the reaction interface, and the grains and pore structures in the refractories mostly maintained their original shapes. It can be observed from Figs. 16 (c) and (d) that some bright substances are dispersed in the matrix and pores. Those bright substances were proved to be Fe element by the energy spectrum analysis, suggesting that the Fe element penetrated into the refractory through the pores and grain boundaries. However, as shown in Table 10, the elemental compositions in CA_6, CA_2 and $CaTiO_3$ have no obvious change, indicating that there is no obvious reaction between the refractory and the molten alloy, except for the penetration of iron element.

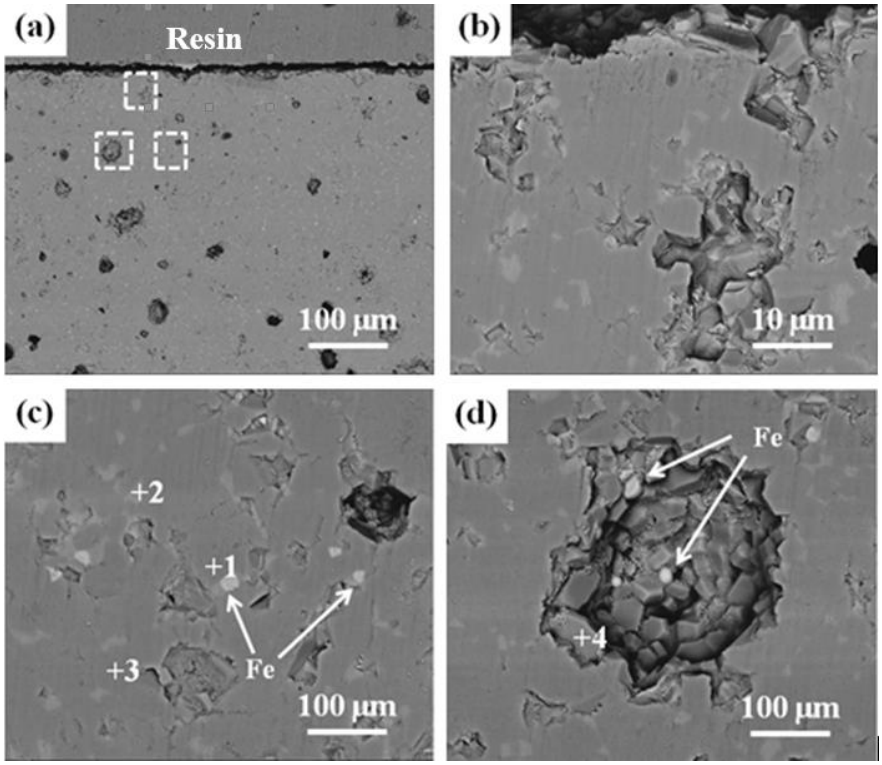

Fig. 16 SEM images of the reaction interface between CA_6-CT refractories and Ti6Al4V melt.

Table 10 EDS analysis of points in Fig. 16 (at.%).

Point	Ca	Al	Ti	O	Possible phase
1	10.7	59.8	2.2	27.3	CA_2
2	24.4	19.1	26.6	29.9	$CaTiO_3$
3	6.9	59.3	2.3	31.5	CA_6
4	6.8	57.1	2.2	33.8	CA_6

4 Conclusion

CA_6-CT materials were prepared using micro $CaCO_3$, nano $CaCO_3$, and $Ca(OH)_2$ as calcium sources. The experimental results showed that the use of different calcium sources had little effect on the phase types and micromorphology of the samples but affected the reaction activity of the reactants. Compared with the samples produced from micro $CaCO_3$ and calcium hydroxide, the pore size of the samples produced from nano $CaCO_3$ after decomposition was smaller; moreover, the higher reaction activity of the generated CaO promoted the development and growth of CA_6 and $CaTiO_3$. Nano $CaCO_3$ is therefore the most suitable calcium source for preparing CA_6-CT materials.

By adjusting the amount of TiO_2, the formation temperature of CA_6 and the sintering temperature of the material can be reduced and the CA_6 grains modified from a plate to an equiaxed morphology, which increases the volume density and decreases the porosity. As the TiO_2 content increases, the sintering temperature of the material gradually decreases. The unstable compound $Ca_3Ti_8Al_{12}O_{37}$ produced when excessive TiO_2 is added may form a liquid phase at high temperatures and adversely affect the sample. The phases of the three groups of samples with added TiO_2 and heat-treated at 1700 °C are stable. Because an excessively high heat-treatment temperature increases the apparent

porosity and loosens the microstructure of the material, the appropriate heat treatment temperature for the samples is 1650 °C.

The volume density of the CA_6-CT material prepared in the experiment was between 3.3 and 3.4 g/cm^3, and its apparent porosity between 7 and 10 %. The material has low thermal conductivity. The thermal conductivity at 800 °C is 2.4–2.8 W/(m·K). The average linear expansion coefficient in the range 25–1000 °C is 7.9×10^{-6}–9.0×10^{-6}/°C, which is between those of Al_2O_3 and ZrO_2. Increasing the TiO_2 content increases the average linear expansion coefficient of the material, which is detrimental to its high-temperature volume stability and thermal shock stability. The CA_6-CT refractory showed good corrosion resistance to the Ti6Al4V melt. Except for a slight penetration of iron element, no obvious corrosion occurred at the reaction interface.

Acknowledgements

The authors are thankful for the financially support from the National Natural Science Foundation of China (Grant No. 52172023, 51902231, 52002295), the Hong Kong Scholars Program 2020 (Grant No. G-YZ4E/ XJ2020023) and the Postdoctoral Science Foundation of Jinan City 2021.

References

[1] A. Saurabh, C.M. Meghana, P.K. Singh, P.C. Verma, Titanium-based materials: synthesis, properties, and applications, Mater. Today 56 (2022) 412-419.

[2] P. Pushp, S.M. Dasharath, C. Arati, Classification and applications of titanium and its alloys, Mater. Today 54 (2022) 537-542.

[3] Q.Y. Zhao, Q.Y. Sun, S.W. Xin, Y.N. Chen, C. Wu, H. Wang, J.W. Xu, M.P. Wan, W.D. Zeng, Y.Q. Zhao, High-strength titanium alloys for aerospace engineering applications: A review on melting-forging process, Mater. Sci. Eng. A 845 (2022) 143260.

[4] D. Wimler, J. Lindemann, M. Reith, A. Kirchner, M. Allen, W.G. Vargas, M. Franke, B. Klöden, T. Weißgärber, V. Güther, M. Schloffer, H. Clemens, S. Mayer, Designing advanced intermetallic titanium aluminide alloys for additive manufacturing, Intermetallics 131 (2021) 107109.

[5] M.R.S.N. Hazwani, L.X. Lim, Z. Lockman, H. Zuhailawati, Fabrication of titanium-based alloys with bioactive surface oxide layer as biomedical implants: Opportunity and challenges, Trans. Nonferrous Met. Soc. China 32 (2022) 1-44.

[6] R.P. Liu, M.Z. Ma, X.Y. Zhang, New development of research on casting of bulk amorphous alloys, Acta Metall. Sin. 57 (2021) 515–528.

[7] X. Ren, J. Xiao, Study on vacuum induction melting process of Superalloy, World nonferrous metal 10 (2018) 18, 21.

[8] A. Lasalmonie, Intermetallics: why is it so difficult to introduce them in gas turbine engines, Intermetallics 14 (2006) 1123–1129.

[9] X.H. Wu, Review of alloy and process development of TiAl alloys, Intermetallics 14 (2006) 1114–1122..

[10] A. Kostov, B. Friedrich, Predicting thermodynamic stability of crucible oxides in molten titanium and titanium alloys, Computational Materials Science 38 (2006) 374-385.

[11] J. Lapin, Z. Gabalcova, Solidification behaviour of TiAl-based alloys studied by

directional solidification technique, Intermetallics 19 (2011) 797-804.

[12] T. Tetsui, T. Kobayashi, T. Mori, T. Kishimoto, H. Harada, Evaluation of Yttria Applicability as a Crucible for Induction Melting of TiAl Alloy, Mater. Trans. 51 (2010) 1656-1662.

[13] T. Tetsui, T. Kobayashi, A. Kishimoto, H. Harada, Structural optimization of an yttria crucible for melting TiAl alloy. Intermetallics 20 (2012) 16-23.

[14] B.G. Fu, H.W. Wang, C.M. Zou, P Ma, Z.J. Wei, Interfacial reactions between Ti-1100 alloy and CaO crucible during casting process, Nonferrous Met. Soc. China 24 (2014) 3118-3125.

[15] Q. Jia, Y.Y. Cui, R. Yang. Intensified interfacial reactions between gamma titanium aluminide and CaO stabilised ZrO_2. Int J Cast Met Res 17 (2004) 23–28.

[16] H.R. Zhang, X.X. Tang, C.G. Zhou, Comparison of directional solidification of γ-TiAl alloys in conventional Al_2O_3 and novel Y_2O_3-coated Al_2O_3 crucibles, J. Eur. Ceram. Soc. 33 (2013) 925-934.

[17] G.Y. Chen, J.Y. Kang, B.B. Lan, P.Y. Gao, X.G. Lu, C.H. Li, Evaluation of Ca-doped $BaZrO_3$ as the crucible refractory for melting TiAl alloys, Ceram. Int. 44 (2018) 12627-12633.

[18] S. Schafföner, C.G. Aneziris, H. Berek, J. Hubálková, B. Rotmann, B. Friedrich, Corrosion behavior of calcium zirconate refractories in contact with titanium aluminide melts, J. Eur. Ceram. Soc. 35 (2015) 1097-1106.

[19] G.Y. Chen, F.H. Yu, X. Hou, J. Liu, Y.C. Yang, E.H. Wang, Q.S. Feng, B.H. Duan, X.G.

Lu, X.M. Hou, C.H. Li, $BaZrO_3$ refractory crucibles for vacuum induction melting of industrial Zr-based bulk metallic glass master alloys with Y addition, J. Eur. Ceram. Soc. 42 (2022) 3644-3651.

[20] B.H. Duan, Q.S. Feng, L.N. Jiao, X.X. Zhang, L. Mao, F.H. Xiong, Y.C. Yang, X.G. Lu, G.Y. Chen, C.H. Li, Failure mechanism of the Y_2O_3 doped $BaZrO_3/Al_2O_3$ composite ceramic mould during directional solidification of TiAl-Based alloys, Ceram. Int. 48 (2022) 4464-4473.

[21] P.E.D. Morgan, M.S. Koutsoutis, Phase relations in the Ca-Ti-Al-O system; further studies on members of the CTA family, J. Mater. Sci. Lett. 4 (1985) 321-323.

[22] K.T. Jacob, G. Rajith, Gibbs energy of formation of $Ca_3Ti_8Al_{12}O_{37}$ and phase relations and chemical potentials in the system Al_2O_3-TiO_2-CaO, J. Phase Equilib. Diff. 33 (2012) 293-302.

[23] J.H. Chen, H.Y. Chen, W.J. Mi, Z. Cao, B. Li, C.J. Liang, Substitution of Ba for Ca in the Structure of $CaAl_{12}O_{19}$, J. Am. Ceram. Soc. 100 (2017) 413-418.

[24] M. Rizwan, Z. Usman, M. Shakil, S.S.A. Gillani, S. Azeem, H.B. Jin, C.B. Cao, R.F. Mehmood, G. Nabi, M.A. Asghar, Electronic and optical behaviour of lanthanum doped $CaTiO_3$ perovskite, Mater. Res. Express 7 (2020) 015920.

[25] R. Salomão, V.L. Ferreira, L.M.M. Costa, I.R.D. Oliveira, Effects of the initial CaO-Al_2O_3 ratio on the microstructure development and mechanical properties of porous calcium hexaluminaten, Ceram. Int. 44 (2018) 2626-2631.

[26] R.L. Neto, T.P. Duarte, J.L. Alves, T.G. Barrigana, S.L. Da, The influence of face coat

material on reactivity and fluidity of the Ti6Al4V and TiAl alloys during investment casting, Proceedings of the Institution of Mechanical Engineers Part L 231 (2017) 38-48.

[27] Z.Y. Wang, J.L. Zhang, Z.J. Liu, G.W. Wang, K.X. Jiao, K.J. Li, T.J. Yang, Production of ferrotitanium alloy from titania slag based on aluminothermic reduction, J. Alloys Compd. 810 (2019) 151969.